

MHD Accretion-Disk Winds as X-ray Absorbers in AGNs

KEIGO FUKUMURA^{1,2,3}, DEMOSTHENES KAZANAS³, IOANNIS CONTOPOULOS⁴,

AND

EHUD BEHAR^{3,5,6}

ABSTRACT

We present the two-dimensional (2D) ionization structure of self-similar magnetohydrodynamic (MHD) winds off accretion disks around irradiated by a central X-ray point source. Based on earlier observational clues and theoretical arguments, we focus our attention on a subset of these winds, namely those with radial density dependence $n(r) \propto 1/r$ (r is the spherical radial coordinate). We employ the photoionization code **XSTAR** to compute the ionic abundances of a large number of ions of different elements and then compile their line-of-sight (LOS) absorption columns. We focus our attention on the distribution of the column density of the various ions as a function of the ionization parameter ξ (or equivalently r) and the angle θ . Particular attention is paid to the absorption measure distribution (AMD), namely their Hydrogen-equivalent column per logarithmic ξ interval, $dN_H/d\log\xi$, which provides a measure of the winds' radial density profiles. For the chosen density profile $n(r) \propto 1/r$ the AMD is found to be independent of ξ , in good agreement with its behavior inferred from the X-ray spectra of several active galactic nuclei (AGNs). For the specific wind structure and X-ray spectrum we also compute detailed absorption line profiles for a number of ions to obtain their LOS velocities, $v \sim 100 - 300 \text{ km s}^{-1}$ (at $\log\xi \sim 2 - 3$) for Fe XVII and $v \sim 1,000 - 4,000 \text{ km s}^{-1}$ (at $\log\xi \sim 4 - 5$) for Fe XXV, in good agreement with the observation. Our models describe the X-ray absorption properties of these winds with only *two parameters*, namely the mass-accretion rate \dot{m} and LOS angle θ . The probability of obscuration of the X-ray ionizing source in these winds decreases with increasing \dot{m} and increases steeply with the LOS inclination angle θ . As such, we concur with previous authors that these

¹Email: Keigo.Fukumura@nasa.gov

²University of Maryland, Baltimore County (UMBC/CRESST), Baltimore, MD 21250

³Astrophysics Science Division, NASA/Goddard Space Flight Center, Greenbelt, MD 20771

⁴Research Center for Astronomy, Academy of Athens, Athens 11527, Greece

⁵Department of Physics, Technion, Haifa 32000, Israel

⁶Senior NPP Fellow

wind configurations, viewed globally, incorporate all the requisite properties of the parsec scale “torii” invoked in AGN unification schemes. We indicate that a combination of the AMD and absorption line profile observations can uniquely determine these model parameters and their bearing on AGN population demographics.

Subject headings: accretion, accretion disks — galaxies: active — methods: numerical — quasars: absorption lines — X-rays: galaxies

1. Introduction

The issue of accretion as the power source behind Active Galactic Nuclei (AGNs) was decided as early as 1969 (Lynden-Bell 1969). Since then, a 40-year effort to unravel the physics underlying this process has produced a great body of observational and theoretical work covering a host of the AGN properties and phenomena. However, due to the small angular size of a black hole horizon, whether at the galactic or extragalactic setting, these studies were effectively performed mainly in the spectral (but also the time) domain; the spatial structure of accretion flows, but those of scale of many parsecs, was then inevitably delegated to models, whose validity was determined by their ability to reproduce the spectral and timing observations with sufficient accuracy. At the risk of oversimplifying the issue, the spectral properties of AGNs were basically outlined (among other works) in Sanders et al. (1989) who showed that the Spectral Energy Distribution (SED) of AGNs includes three broad components in the IR, optical-UV and X-ray bands, with roughly equal energy per decade, with the radio comprising only a small fraction of their bolometric luminosity, of order $\sim 10^{-6}$ in the Radio-Quiet (RQ) AGNs and $\sim 10^{-3}$ in Radio-Loud (RL) AGNs.

Considering that accretion produces most of its power in the last 10 or so Schwarzschild radii, r_S , outside the black hole horizon, barring an inherently non-thermal emission process (as it turns out to be the case with blazars), it is strange that the observed SEDs exhibit roughly constant luminosity per decade. Interestingly, the simplest of assumptions, namely radiation of the AGN bolometric luminosity in black body form by an object (most likely in the form of a cold disk of $T \sim 10^4 - 10^6$ K) of size a few r_S of a supermassive black hole ($M \sim 10^6 - 10^8 M_\odot$ where M_\odot is the solar mass), implies peak emission at UV frequencies, consistent with the observationally identified UV feature referred to above, known as the Big Blue Bump (BBB); as such, this feature was modeled with emission by a geometrically-thin, optically-thick accretion disk extending usually to the Innermost Stable Circular Orbit (ISCO) of the black hole. Of the other two distinct components the X-rays are generally attributed to emission by an optically-thin, hot ($T \sim 10^8 - 10^9$ K) corona overlying this disk and heated by the action of magnetic fields that thread the geometrically-thin disk, in close analogy to the Solar Corona (e.g. Haardt & Maraschi 1991; Kawanaka, Kato, & Mineshige

2008). Finally, the IR emission was accounted for as the result of reprocessing the O-UV radiation by a geometrically thick (scale height h roughly equal to the local radius r , i.e. $h \sim r$), cool, molecular torus at large distances ($\gtrsim 1$ pc) from the central engine [an arrangement that presents a bit of a problem, since the temperature of this torus ($\sim 10 - 100$ K) is much less than the virial temperature of the gas at that distance and would lead to a configuration with $h \ll r$; see Krolik & Begelman (1988)]. The region between the torus and the accretion disk was thought to be occupied by clouds with velocity widths ranging from tens of thousands to several hundreds of kilometers per second, producing the observed line radiation, with the ensemble of these components encapsulated in the well known cartoon of Urry & Padovani (1995).

While in most models these components are generally thought of as independent, Principal Component Analysis (PCA) of multiwavelength AGN features by Boroson & Green (1992) and Boroson (2002) indicated that most of the variance in the measured optical emission line properties and a broad range of continuum features (radio, optical, X-ray) of AGNs was contained in two sets of correlations, eigenvectors of the correlation matrix. This analysis suggested that the properties of these features are not independent (despite their diverse locations and emission processes) but are well correlated by two single underlying physical parameters through the physics of accretion and the conversion of its power to radiation and outflows. On the other hand, general theoretical arguments suggesting, e.g. a tight correlation between variations in the X-ray and O-UV components, given their implied proximity, were not confirmed by observations (Nandra et al. 1998).

The advent of X-ray instrumentation and in particular X-ray spectroscopy, established the presence of spectral components apparently present across the entire range of compact object masses from galactic black hole candidates (GBHCs) to luminous AGNs, namely outflowing X-ray absorbing matter in our line of sight (LOS) manifested as complex (blueshifted) absorption features of hydrogen equivalent column density $N_H \sim 10^{21} - 10^{23} \text{ cm}^{-2}$. The presence of this absorbing material, often referred to as Warm Absorber, was first established in *ASCA* observations of many AGNs (e.g. Reynolds and Fabian 1995) and GBHCs (e.g. Miller et al. 2006) which provided clear evidence of highly ionized oxygen O VII (0.739 keV) and/or O VIII (0.871 keV) along the LOS. More recently, grating spectra of high-resolving power obtained by *Chandra* and *XMM-Newton* have enabled the study of these absorption features in greater detail leading to the conclusion that they are present in a large fraction of AGNs and span a wide range ($\sim 10^5$) in ionization parameter (e.g. Holczer, Behar & Kaspi 2007, hereafter HBK07). Some sources appear to contain low and/or high velocity outflows (e.g. HBK07; Holczer, Behar & Arav 2009) while a handful of objects exhibit a trans-relativistic outflow (e.g. Chartas et al. 2009; Pounds & Reeves 2009; Reeves et al. 2009). In addition in both AGNs and GBHCs the observed outflows from at least a number of sources have been suggested to be accelerated magnetically (rather than by another process) off an accretion disk (e.g., see Miller et al. 2006, 2008 for GRO J1655-40; Kraemer et al. 2005 and

Crenshaw & Kraemer 2007 for NGC 4151). A brief review of luminous AGN winds is found in Brandt et al. (2009). These facts imply the presence of gas covering a large fraction of the solid angle and distributed over a large range of radii, perhaps the entire range between the X-ray source and the torus, indicating AGNs to be multiscale and multiwavelength objects rather than a class with properties determined only by the power released by accretion in the black hole vicinity. This last point has gained further support with the discovery of the correlation between the accreting black hole mass and the velocity dispersion of the surrounding stellar population (Ferrarese & Merrit 2000).

From the theoretical point of view, most early AGN treatments were focused on the structure of the innermost regions of the accretion flow and as such they limited themselves to the study of the conditions in a rather narrow range of radii. Nonetheless, several treatments of magnetohydrodynamic (MHD) accretion disk winds, aiming to account for the observed AGN outflows, employed self-similar solutions, which naturally span a large range in radius (e.g. Blandford & Payne 1982, hereafter BP82; Contopoulos & Lovelace 1994, hereafter CL94). Using the structure of these solutions, Königl & Kartje (1994, hereafter KK94) proposed that the so-called molecular torus of the AGN unification scheme is a dynamical rather than a static object, namely an MHD wind of the type suggested in the above works. KK94 also contented that agreement between model and observation demanded a rather specific type of wind, a particular case of those discussed in CL94, one that we also concentrate on in the present work. At the same time, they noted that the 2D geometry of these winds (with low column at inclination angles $\theta \simeq 0^\circ$, i.e. along the wind axis, and high column at $\theta \simeq 90^\circ$) provided, in addition, a natural framework for the unification scheme of type I and II Seyfert galaxies proposed by Antonucci & Miller (1985), thereby linking the large scale AGN spectral classification to the dynamics of AGN accretion/outflows.

Self-similar solutions of the accretion flow equations were also provided by Narayan & Yi (1994, 1995a), who considered the structure of hot accretion flows in the regime of low accretion rate, i.e. for accretion rates less than the Eddington value, $\dot{m} \equiv \dot{M}/\dot{M}_E \lesssim 1$. Because for these low rates the accretion time scale τ_{acc} is shorter than the gas cooling time τ_{cool} , in fact $\tau_{acc} \simeq \dot{m} \tau_{cool}$, only a fraction \dot{m} of the energy released in the dissipation of the plasma kinetic energy is radiated away with the remainder advected into the black hole (hence the term Advection Dominated Accretion Flows or ADAFs); as a result, the accretion luminosity is then proportional to \dot{m}^2 (rather than \dot{m}). The high temperature of the inner ADAFs, provides naturally for the hot component required to produce the observed X-ray emission, which, rather than being an independent component, within ADAFs is incorporated in the dynamics of accretion itself (see Narayan & McClintock 2008, for recent review). More recently, Blandford & Begelman (1999), elaborated further on ADAFs elucidating, among others, the reason for which the Bernoulli integral of ADAFs is positive (a point that had been noted by Narayan & Yi 1994, 1995a), that being that the viscous stresses transfer outward, in addition to angular momentum, also mechanical energy. They then proposed that

this excess energy can be carried away in the form of wind over a large range of radii, thereby leading to configurations similar to those obtained in the more detailed studies of BP82 and CL94, while at the same time maintaining some of the general properties of ADAFs. The combination of radiatively inefficient flows with the simultaneous presence of winds led to the nomenclature Advection Dominated Inflow-Outflow Solutions (ADIOS). Following these pioneering works, many attempts have been made in recent years to reproduce and explain the kinematics and X-ray spectra of the observed outflows in AGNs (see, among others, Proga 2003; Everett 2005; Sim 2005; Schurch & Done 2007; Dorodnitsyn, Kallman & Proga 2008; Sim et al. 2008; Schurch, Done & Proga 2009).

Motivated by these considerations we are taking a closer look at the issue of Warm Absorbers (X-ray absorbing medium) in terms of specific disk-wind models, namely those of CL94. As it will be discussed in more detail later on, these solutions are characterized by a parameter q , which determines the distribution of axial current in the wind as a function of the radius; this parameter, in conjunction with the MHD conservation laws and the radial force balance, determines both the radial dependence of the matter density in the wind and the radial dependence of the toroidal magnetic field component B_ϕ . Taking our lead from the works of Behar et al. (2003) and HBK07, in the present work we restrict our attention to wind models with $q = 1$, i.e. the value used also by KK94. This is in a sense a critical value of this parameter because, as discussed in CL94, it leads to winds with toroidal magnetic field $B_\phi \propto 1/r$ and therefore magnetic field energy on the disk that diverges only logarithmically at small and large r and as such it can be considered as a “minimum magnetic energy” configuration (KK94); values of $q \neq 1$ lead to configurations with power-law divergence either at small or large R . In addition, the choice $q = 1$ leads to a wind with radial density profile $n(r) \propto r^{-1}$, i.e. a profile with equal column per logarithmic radial interval (and normalization that depends on the polar angle θ and the mass-accretion rate \dot{m}), a fact that is in general agreement with the profiles implied by the ionized absorbers data analysis to date (HBK07). It is worth noting that a similar density profile was invoked by Kazanas, Hua & Titarchuk (1996) and Hua, Kazanas & Titarchuk (1997) to explain the Fourier frequency dependence of the soft-hard X-ray lags observed in GBHCs and in AGNs (Papadakis et al. 2002).

With the wind 2D (r and θ) density field as a function of radius and angle provided by the models of CL94 (i.e. ignoring at present effects that can be attributed to other agents that could affect the wind structure) and the assumption of a point X-ray source of a given spectrum at the origin, one can compute their 2D ionization structure and in particular the local column density of specific ionic species as a function of radius and angle. One can also compute the integrated column of each such ion, quantities that can be directly compared to observation (HBK07). This we do in the present work. While a number of issues remain open or are sidestepped in the present self-similar wind models, this is the price to pay in order to limit the number of free parameters to just two (the wind mass flux and the observer

inclination angle), a fact that allows the study of the properties of warm absorbers within the global perspective of AGN unification.

Our paper is structured as follows: in §2 we review the MHD wind equations and structure as given in CL94 and make a connection of these winds with flows of the ADAF/ADIOS type by relating the wind density normalization to the ionizing luminosity produced by the idealized point source at the coordinate origin. In §3 we provide the general 2D ionization structure, the local column of specific ions as a function of radius as well as the total ionic column of a given charge state and for each element, as well as the absorption line profiles of selected transitions. In §4 the results are compared to observation, the properties and limitation of the present treatment are discussed and a course for future work is charted.

2. Description of the Model

Our wind model consists primarily of two parts: *(i)* The outflow/wind structure originating from a geometrically-thin accretion disk as described by CL94 and *(ii)* The computation of the ionization of the wind plasma under local heating-cooling and ionization equilibrium, by employing the photoionization code **XSTAR** (Kallman & Bautista 2001). These two steps are self-consistently coupled in a scheme similar to some previous work in a slightly different context (e.g. Schurch & Done 2007; Dorodnitsyn, Kallman & Proga 2008; Schurch, Done & Proga 2009). All calculations are performed under steady-state, axisymmetric conditions as shall be described in detail in the following sections.

2.1. Self-similar MHD Wind from Accretion Disks

While the detailed formalism of self-similar MHD wind solutions is found in CL94, let us here briefly summarize some of their characteristics. The basic equations of this problem are those of steady-state, nonrelativistic, ideal MHD that include gravity and gas pressure, namely

$$\nabla \cdot (\rho \mathbf{v}) = 0 \quad (\text{mass conservation}) , \quad (1)$$

$$\nabla \times \mathbf{B} = \frac{4\pi}{c} \mathbf{J} \quad (\text{Ampere's law}) , \quad (2)$$

$$\mathbf{E} + \frac{\mathbf{v}}{c} \times \mathbf{B} = 0 \quad (\text{ideal MHD}) , \quad (3)$$

$$\nabla \times \mathbf{E} = 0 \quad (\text{Faraday's law}) , \quad (4)$$

$$\rho(\mathbf{v} \cdot \nabla) \mathbf{v} = -\nabla p - \rho \nabla \Phi_g + \frac{1}{c} (\mathbf{J} \times \mathbf{B}) \quad (\text{momentum conservation}) , \quad (5)$$

$$\nabla \cdot \mathbf{B} = 0 \quad . \quad (6)$$

Here, the plasma wind velocity \mathbf{v} is assumed to be frozen into the global magnetic field \mathbf{B} ; \mathbf{E} is the electric field; \mathbf{J} is the electric current density; and c is the speed of light. The gas pressure p and mass density ρ of the wind are related through an equation of state

$$p = K\rho^\Gamma, \quad (7)$$

where K and Γ are the adiabatic constant and adiabatic index respectively. The assumption of axial symmetry allows one to separate poloidal quantities from toroidal ones as $\mathbf{B} = \mathbf{B}_p + \mathbf{B}_\phi$ and $\mathbf{v} = \mathbf{v}_p + \mathbf{v}_\phi$, with

$$\mathbf{B}_p = \frac{1}{r \sin \theta} \nabla \Psi \times \hat{\phi}, \quad (8)$$

where, $\Psi(r, \theta)$ is the magnetic flux function. We will henceforth work in spherical coordinates (r, θ, ϕ) [note that CL94 used cylindrical ones (R, ϕ, Z)]. Magnetic field lines lie along surfaces of constant value of Ψ . Furthermore, under conditions of steady-state, the following quantities are conserved along field lines characterized by the value of Ψ

$$4\pi\rho \frac{v_p}{B_p} \equiv F(\Psi), \quad (9)$$

$$\frac{1}{r \sin \theta} \left(v_\phi - \frac{F}{4\pi\rho} B_\phi \right) \equiv \Omega(\Psi), \quad (10)$$

$$r \sin \theta (B_\phi - v_\phi F) \equiv H(\Psi), \quad (11)$$

$$\int_{\Psi=\text{const}} (d\rho/\rho) + \frac{1}{2}v^2 + \Phi_g - r \sin \theta v_\phi \Omega \equiv J(\Psi), \quad (12)$$

$$k_B (\Gamma - 1)^{-1} \ln(K) \equiv S(\Psi), \quad (13)$$

where $F(\Psi)$ is the ratio of mass to magnetic fluxes, $\Omega(\Psi)$ is the angular velocity of magnetic field lines, $H(\Psi)$ corresponds to the specific angular momentum (it includes magnetic torques), $J(\Psi)$ is the specific energy (Bernoulli) integral, and $S(\Psi)$ is the specific entropy. Also, k_B is Boltzmann's constant, and Φ_g is the Newtonian gravitational potential. The wind velocity field \mathbf{v} is related to the magnetic field \mathbf{B} as

$$\mathbf{v} = r \sin \theta \Omega \hat{\phi} + \frac{F}{4\pi\rho} \mathbf{B}. \quad (14)$$

CL94 first showed that one can obtain general self-similar solutions of the above system of equations of the form

$$\mathbf{B}(\mathbf{r}, \theta) \equiv (r/r_o)^{q-2} \mathbf{b}(\theta) B_o, \quad (15)$$

$$\mathbf{v}(\mathbf{r}, \theta) \equiv (r/r_o)^{-1/2} \mathbf{v}(\theta) v_o, \quad (16)$$

$$p(r, \theta) \equiv (r/r_o)^{2q-4} \mathcal{P}(\theta) B_o^2, \quad (17)$$

$$\rho(r, \theta) \equiv (r/r_o)^{2q-3} \mathcal{R}(\theta) B_o^2 v_o^{-2}. \quad (18)$$

Here, r_o is the launch radius of a characteristic field/flow line at the base of the wind at $\theta = 90^\circ$ while B_o and v_o are respectively the magnitude of the vertical components of the magnetic field and the initial rotational wind velocity at the same foot point; $\mathbf{b}(\theta)$ and $\mathbf{v}(\theta)$ are dimensionless with $b_z(90^\circ) = v_\phi(90^\circ) \equiv 1$ while $\mathcal{P}(\theta)$ and $\mathcal{R}(\theta)$ denote the angular dependence of the pressure and wind density, respectively. The exponent q is a free parameter that controls the radial scaling of the magnetic field. One sees directly that q discriminates current-carrying wind configurations (when $q > 1$, rB_ϕ grows with r ; the wind carries a net axial current) from zero-total-current ones (when $q < 1$, $rB_\phi \rightarrow 0$ for $r \rightarrow \infty$; the wind carries a singular axial current and its corresponding return current; see CL94 and references). Obviously,

$$\Psi(r, \theta) = (r/r_o)^q \psi(\theta) \Psi_o, \quad (19)$$

where $\psi(\theta)$ is dimensionless, $\psi(90^\circ) = 1$, and $\Psi_o \equiv B_o r_o^2 b_z(90^\circ) q^{-1}$ is the poloidal magnetic flux through radius r_o . The above scalings allow us to obtain the geometry of the poloidal field/flow lines (characterized by the value of Ψ) as

$$r|_\Psi(\theta) \equiv r_o (\Psi/\Psi_o)^{1/q} \psi(\theta)^{-1/q}. \quad (20)$$

Note that the function $\psi(\theta)$ characterizes the shape of all field/flow lines. That is, all field/flow lines are self-similar to the ‘characteristic’ field/flow line that originates at $r = r_o$ and $\theta = 90^\circ$ on the disk. Self-similarity further implies that

$$F(\Psi) = (\Psi/\Psi_o)^{1-3/2q} F_o B_o v_o^{-1}, \quad (21)$$

$$\Omega(\Psi) = (\Psi/\Psi_o)^{-3/2q} \Omega_o v_o r_o^{-1}, \quad (22)$$

$$H(\Psi) = (\Psi/\Psi_o)^{1-1/q} H_o B_o r_o, \quad (23)$$

$$J(\Psi) = (\Psi/\Psi_o)^{-1/q} J_o v_o^2, \quad (24)$$

$$S(\Psi) = k_B (\Gamma - 1)^{-1} [\{(2 - 4/q) - \Gamma(2 - 3/q)\} \ln(\Psi/\Psi_o) + \ln \mathcal{K}], \quad (25)$$

where $\mathcal{K} = \mathcal{P}(\theta)/\mathcal{R}(\theta)^\Gamma$ is a dimensionless adiabatic constant. The adiabatic speed of sound scales as

$$c_s(r, \theta) \equiv \left(\frac{\partial p}{\partial \rho} \right)_{\Psi=const.}^{1/2} = (\Psi/\Psi_o)^{-1/2q} \left[\mathcal{K} \Gamma \mathcal{R}(\theta)^{\Gamma-1} \right]^{1/2} v_o = (\Psi/\Psi_o)^{-1/2q} c_s(\theta) v_o. \quad (26)$$

Finally, one can combine the dimensionless forms of equations (9)-(25) that involve the dimensionless quantities (\mathbf{v} , \mathbf{b} , \mathcal{P} , \mathcal{R} , c_s) as functions of θ , and thus express the poloidal projection of the momentum balance equation (5) [the so called generalized Grad-Shafranov (GS) equation] in the form of a second-order ordinary differential equation for $\psi(\theta)$ as

$$\psi''(\theta) = f(\theta, \psi, \psi'). \quad (27)$$

This equation (too complicated to write down explicitly in this paper) is integrated numerically from the surface of the disk (taken for simplicity to lie at $\theta = 90^\circ$) to axial infinity ($\theta = 0^\circ$). The initial conditions are $\psi(90^\circ) = 1$ and $\psi'(90^\circ)$, essentially a free-parameter that depends on the details of the internal disk structure, which, for a given value of H_o , is adjusted in order for the wind to cross the Alfvén point (the point at which the the wind poloidal speed v_p becomes equal to the local Alfvén speed - see CL94 for a detailed description) continuously and smoothly. According to equation (20), the form of the solution $\psi(\theta)$ characterizes the poloidal shape of the field lines, and in particular, the initial condition $\psi'(90^\circ)$ characterizes the angle the poloidal field/flow lines make with the disk at their foot points [readers can easily verify that this angle is equal to $\tan^{-1}\{q/\psi'(90^\circ)\}$].

To numerically solve the above wind equation (27) we assume that the plasma is initially in Keplerian rotation $v_o \equiv v_\phi(90^\circ) = v_K$ at the disk surface ($\theta = 90^\circ$) with only a small out-of-the-disk velocity component ($v_r, v_\theta \ll v_\phi$ at 90°). As a fiducial solution we fix the following set of parameters as described in CL94; $q = 1$, $F_o = 0.15$, $H_o = -1.584$ with kinematic variables $v_\phi(90^\circ) = 1$, $v_\theta(90^\circ) = 0.01$, $\mathcal{K} = 0.01$ and $\Gamma = 5/3$. With these initial conditions, the remaining conserved quantities are calculated as $\Omega_o = 1 - v_\theta(90^\circ)(F_o + H_o) = 0.983$, and $J_o = v_\theta^2(90^\circ)[1 + (\psi'(90^\circ))^2]/2 - 1/2 - \Omega_o \sim -1.483$ (see CL94 for details). The only freedom left is the value of $\psi'(90^\circ)$ that is obtained iteratively so that the wind passes smoothly through the Alfvén surface. This important physical constraint yields $\psi'(90^\circ) = 0.98091$. Note that for sufficiently small F_o (a magnetically dominated flow) its velocity is nearly Keplerian, setting the value of Ω_o , while passing through the Alfvén point fixes H_o and effectively the remaining constants of the flow, with q as the one meaningful free parameter. The obtained wind kinematics are shown in Figure 1a and the magnetic field components in Figure 1b. As discussed in CL94, different values of the exponent q allow for distinct streamline geometries in the poloidal plane, which in turn is associated with other observable quantities of the wind (such as the density profile; see following sections). As is initially set up, this wind is launched from a thin Keplerian disk with only a small out-of-the-disk surface velocity component. The magnetic field there is dragged by the rotating plasma ($v_\phi > 0$) resulting thus in a negative toroidal field component ($B_\phi < 0$). As the wind leaves the disk, magnetic torques act on the outflowing plasma and magnetic energy is efficiently converted into kinetic energy of the wind along the symmetry axis. The magnetic field also plays an important role in collimating the wind at large distances. In this particular case the wind is found to end up with terminal velocity roughly a few times the initial rotational speed and remains below fast magnetosonic speed.

The astute reader may note that X-ray heating is likely to produce thermal velocities inconsistent with the self-similarity of the sound speed invoked above (i.e. $c_s^2 \propto 1/x$; see Fig. 4). We will discuss this in §3.1.

Knowing the wind streamline described by equation (27) one can separately write down

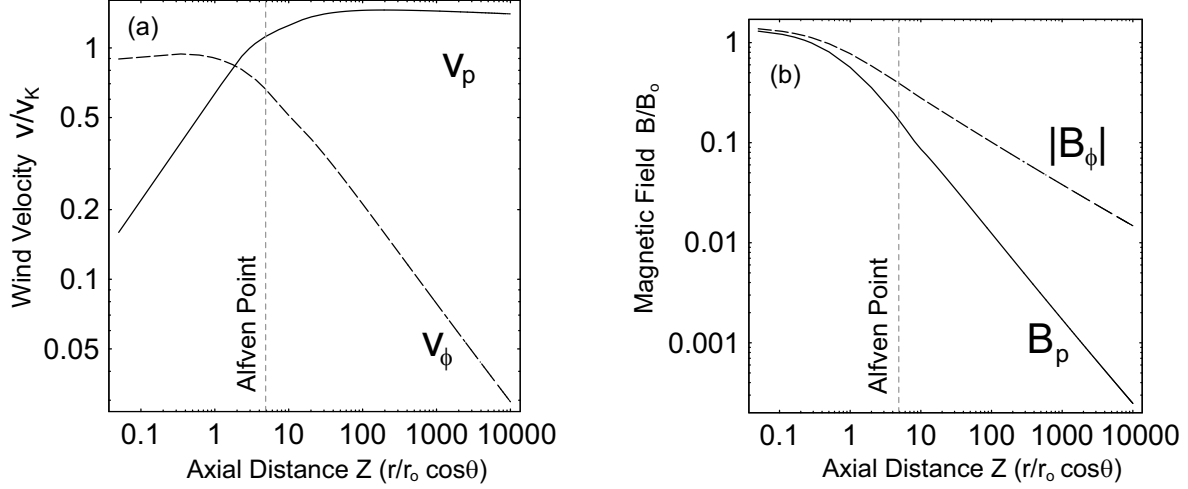


Fig. 1.— MHD wind solution of the GS-equation (27) in the poloidal plane: (a) poloidal v_p (solid) and toroidal v_ϕ (dashed) velocities (in units of $v_o = v_K$) as a function of axial distance $Z \equiv (r/r_o) \cos \theta$ and (b) poloidal B_p (solid) and toroidal $|B_\phi|$ (dashed) magnetic fields (in units of B_o) also as a function of Z along the characteristic field/flow line originating at $r = r_o$ on the disk for the parameters described in the text. Note that we show the absolute value of $B_\phi (< 0)$. Vertical dotted lines denote the axial location of the Alfvén point.

radial and angular dependence of the wind number density $n(r, \theta)$ as

$$n(r, \theta) \equiv \frac{\rho(r, \theta)}{\mu m_p} = n_o x^{2q-3} \mathcal{N}(\theta) , \quad (28)$$

where $n_o \equiv B_o^2 \mathcal{R}(90^\circ) / (\mu m_p v_o^2)$ is the number density normalization at the initial characteristic launching radius r_o , $\mathcal{N}(\theta) \equiv \mathcal{R}(\theta) / \mathcal{R}(90^\circ)$ is the normalized angular dependence of the wind number density, and $x \equiv r/r_o$ is the non-dimensional radial coordinate; m_p is the proton mass and $\mu = 1.26$ the mean molecular weight of the wind. In what follows, we will take the characteristic radius to be equal to the Schwarzschild radius, namely $r_o = r_S$, taken to be the inner edge of the accretion flow with $r_S \simeq 3 \times 10^5 \hat{M}$ cm where $\hat{M} \equiv M/M_\odot$ is the mass of the black hole in units of solar mass M_\odot . It is well known that free-fall spherical accretion at the Eddington rate ($\dot{m} = 1$) produces Thomson opacity one ($\tau_T \simeq 1$) at the Schwarzschild radius ($r \simeq r_S$). Using this scaling we can express our wind density normalization at the inner edge of the disk as

$$n_o = \frac{\eta_W \dot{m}}{2 \sigma_T r_S} , \quad (29)$$

where, η_W is the ratio of the mass-outflow rate in the wind to the mass-accretion rate \dot{m} , assumed here to be $\eta_W \simeq 1$, and σ_T is the Thomson cross-section. It is important to note here that because the mass flux in these winds depends in general on the radius, a

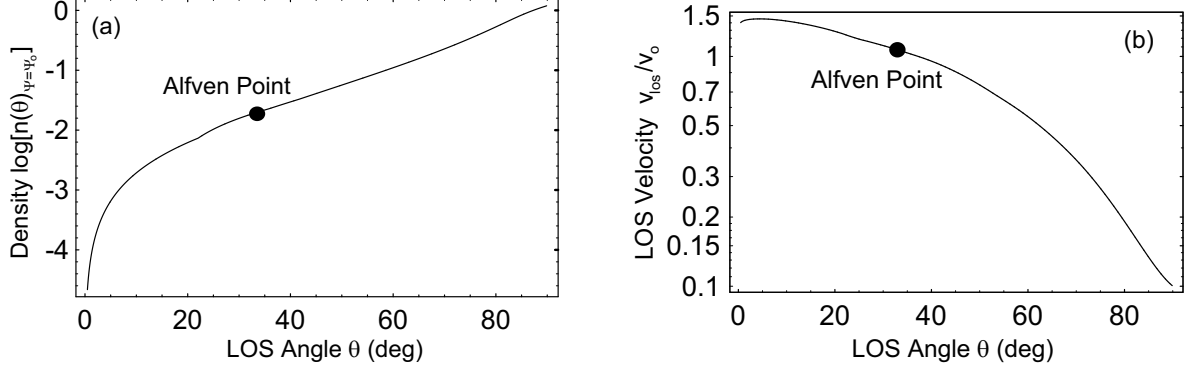


Fig. 2.— Wind properties along a streamline (of $\Psi = \Psi_o$) as a function of LOS angle θ : (a) density profile $n(\theta)_{\Psi=\Psi_o}$ (normalized to unity) given by equation (27). (b) LOS wind velocity v_{los} along the same characteristic field/flow line (in units of $v_o = v_K$ at the base of the wind). A dot denotes the position of the Alfvén point. The parameters are the same as in Figure 1.

normalized parameter used throughout this work, \dot{m} , always refers to the mass flux at the innermost value of the flow radius, i.e. at $x \simeq 1$.

Figure 2a exhibits a LOS angle (θ) dependence of the wind density profile $n(\theta)_{\Psi=\Psi_o}$ from the pole ($\theta = 0^\circ$) to the equator ($\theta = 90^\circ$) along a characteristic stream line of $\Psi = \Psi_o$, normalized to unity at its highest value at $\theta = 90^\circ$, as obtained from the self-similar solution of Figure 1. This distribution illustrates the significant change of the LOS density (and also column density) with inclination angle (over three decades between $5^\circ \lesssim \theta \lesssim 90^\circ$). The LOS wind velocity v_{los} (in units of $v_o = v_K$) along a characteristic streamline is shown in Figure 2b. We see that v_{los} increases as the LOS angle θ becomes smaller (toward the polar region) because the wind is magnetocentrifugally accelerated along the way, and furthermore, the direction of v_{los} becomes more and more parallel to the total wind velocity \mathbf{v} as well [e.g. $v_{\text{los}}(30^\circ) \sim 2v_{\text{los}}(60^\circ)$].

In terms of the scalings of our wind model, the total equivalent hydrogen column density N_H of wind over the LOS length scale of Δr is given by

$$\begin{aligned} N_H(\Delta r, \theta) &\equiv \int_{\Delta r} n(r, \theta) dr \\ &= \eta_W \mathcal{N}(\theta) \frac{\dot{m}}{2\sigma_T} \times \begin{cases} \frac{1}{2(q-1)} x^{2(q-1)} \Big|_{\Delta x} & \text{if } q \neq 1, \\ \ln x \Big|_{\Delta x} & \text{if } q = 1, \end{cases} \end{aligned} \quad (30)$$

where the wind is considered to extend from an inner radius $r = r_{\text{in}} = r_o \simeq r_S$ over a length scale of $\Delta r \equiv \Delta x \cdot r_S$ along the LOS. One should note that the $q = 1$ configurations have the interesting property of equal column density per decade of radius, i.e. $dN_H/d \log r = \text{const} \propto$

$\mathcal{N}(\theta)$ [as can be seen from Fig. 2a, $n(\theta)_{\Psi=\Psi_o} \simeq e^{-(\theta-90^\circ)/13^\circ}$ is an excellent fit to the angular dependence of the density for $\theta \gtrsim 10^\circ$ where θ is measured in degrees]. For $\dot{m} \simeq 1$ and $\theta \simeq 90^\circ$ these winds have a column density of $\simeq 10^{24} \text{ cm}^{-2}$ per decade of radius. As a result, configurations that extend over a number of decades in radius can be quite optically-thick in these directions even for $\dot{m} \ll 1$.

2.2. The Wind Ionization Structure

With the poloidal field configuration obtained by solving equation (27) and the corresponding wind kinematics, we now are in a position to consider its ionization structure assuming the presence of a point-like X-ray source at the origin. To this end we employ the photoionization code **XSTAR** version 2.1kn9, which solves simultaneously for the ionization balance and thermal equilibrium of the locally illuminated wind.

The implementation of the above code involves a number of issues and leads to certain wind observables, amongst which are the following: (i) The ionization is locally determined by the photon flux per electron flux; a proxy for that is the ionization parameter $\xi \equiv L/(nr^2)$, with L being the luminosity of the ionizing source; (ii) The computation of the ionizing flux requires the transfer of radiation from the source through the LOS wind, given that part of it can be removed by scattering and absorption; (iii) Given that our wind models produce, in addition to the density $n(r, \theta)$, also the wind velocity field $\mathbf{v}(\mathbf{r}, \theta)$ we are then able to compute also detailed absorption line profiles; (iv) The broad range of the wind density with radius leads to ions with very diverse ionization states, whose distribution per logarithmic ξ interval, the AMD, discussed in HBK07 and Behar (2009), can be used to determine the wind radial profile. We will discuss each one of these issues in detail below.

2.2.1. The Ionization Parameter

With the density profile at hand, the wind ionization structure, i.e. the local value of ξ , requires also an expression for the X-ray luminosity. Since the models we present are global, i.e. they cover a large number of decades in radius, it makes more sense that we do not detach the ionizing luminosity from the global wind dynamics. In order to do so we need a prescription that connects the wind mass flux rate \dot{m}_w and the ionizing luminosity L . The simplest assumption is that $L \propto \dot{m} = \dot{m}_d = \dot{m}_w$, i.e. to assume that the wind mass rate is proportional to the accretion rate onto the black hole (we assume they are equal), resulting in luminosity L proportional \dot{m} . If this were indeed true, then the ionization structure of the wind would be independent of the accretion rate, since \dot{m} would drop out of the expression for the ionization parameter $\xi = L/nr^2$ [c.f. eqn. (29)]. However, this

is contrary to observations (e.g. Ueda et al. 2003; Tueller et al. 2008), which indicate that the probability of source obscuration decreases with increasing source luminosity (one should note, however, that obscuration may be also due to gas in galactic mergers; e.g. Hopkins et al. 2005). To incorporate this fact, we provisionally adopt the prescription $L \propto \dot{m}^2$, even though any power near 2 or greater would qualitatively suffice. We note that $L \propto \dot{m}^2$ prescription would be appropriate for flows such as those discussed in Narayan & Yi (1995b) (provided that $\dot{m} \lesssim \alpha^2$; α is the usual disk viscosity parameter) with $L \propto \dot{m}$ otherwise; considering that the latter case is valid for only a small range in \dot{m} ($0.1 \lesssim \dot{m} \lesssim 1$) than the former, we adopt the former, bearing in mind its limits of applicability. Expressing the luminosity in terms of its Eddington value we can write

$$L \simeq \epsilon \dot{m}^2 L_0 \hat{M} = 2\pi \epsilon \dot{m}^2 \frac{r_S m_p c^3}{\sigma_T}, \quad (31)$$

where $L_0 \simeq 1.28 \times 10^{38} \text{ erg s}^{-1}$ is the Eddington luminosity of a one solar mass an accreting object and ϵ is the efficiency of conversion of mass into radiation for $\dot{m} = 1$. Given the ionizing luminosity L , and assuming the source to be point-like, located at the coordinate origin, the local value of the ionization parameter (ratio of ionizing flux per electron flux) is

$$\xi(r, \theta) \equiv \frac{L}{n(r, \theta) r^2}. \quad (32)$$

Using the luminosity, density and radius scalings given above this reads as

$$\xi(r, \theta) = \frac{4\pi \epsilon}{\mathcal{N}(\theta) \eta_W} \frac{m_p c^3 \dot{m}}{x^{2q-1}} \simeq \frac{\epsilon}{\mathcal{N}(\theta) \eta_W} \frac{3 \times 10^8 \dot{m}}{x^{2q-1}}. \quad (33)$$

Equation (33) thus provides the explicit dependence of the ionization parameter of the corresponding wind as a function of the accretion rate \dot{m} , the (normalized) distance from the source x and the LOS angle θ for steady-state accretion at a rate \dot{m} into the black hole and actual mass outflow rate (at radius $x \simeq 1$) $\eta_W \dot{m}$ in the wind. Figure 3 shows poloidal color maps of (a) the wind density $n(r, \theta)$ and (b) the ionization parameter $\xi(r, \theta)$ for the parameters used to produce Figure 1 along with a number of contour curves (dotted curves with values) and the flow streamlines (solid curves). The diagonal dashed straight lines denote the self-similar surface of the Alfvén point. Here, we have assumed $M_{BH} = 10^6 M_\odot$ and $L = 3.3 \times 10^{42} \text{ erg s}^{-1}$, which for $\epsilon \simeq 0.2$ implies $\dot{m} \simeq 0.1$. As seen, we obtain a non-recollimating, non-oscillating wind which asymptotically behaves as $r \propto (\cot \theta)^{1/\zeta} \sec \theta$ where $\zeta = \text{const.} \simeq 1/2$ as $r \rightarrow \infty$ [or in cylindrical coordinates (Z, R) $R \propto Z^{1-\zeta}$; see CL94]. We would like to stress that the field line geometry depends on the wind's conserved quantities in the model. As a consequence the obtained wind properties (shown here in Figs. 1 to 3) can change quite a bit.

In the context of our accretion-disk wind scenario the outflows are necessarily more opaque near the launching disk surface ($\theta = 30^\circ$) at smaller radius as expressed in equation (28). Density profile along a magnetic field follows exactly the one shown in Figure 2a.

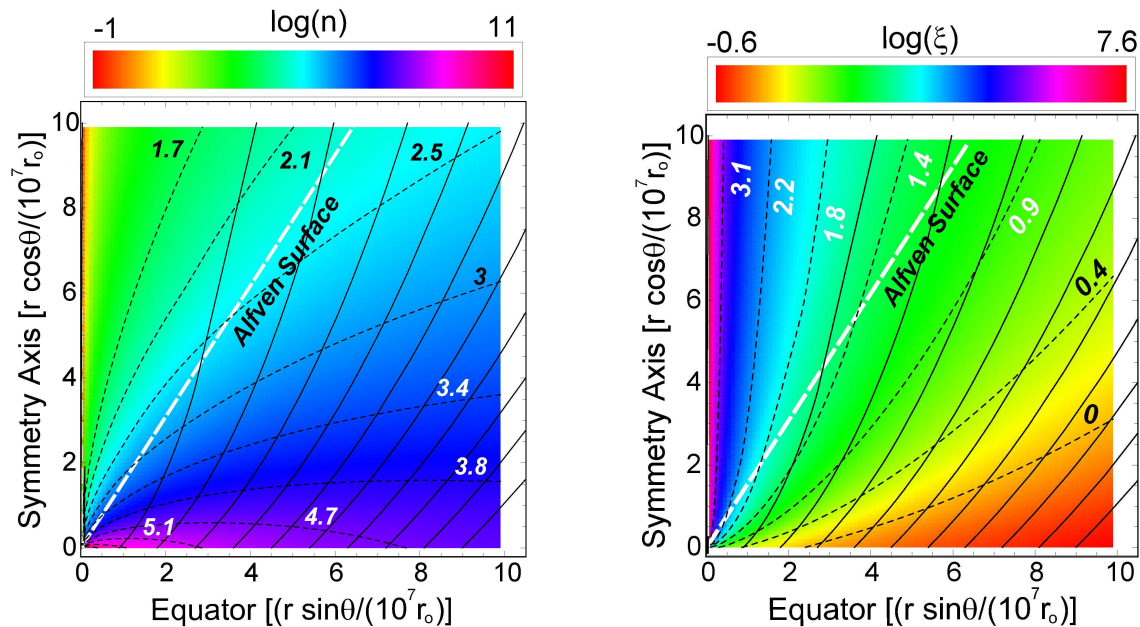


Fig. 3.— Poloidal distribution of (a) the wind density (in units of cm^{-3}) $\log n(r, \theta)$ and (b) the ionization parameter (in units of erg cm s^{-1}) $\log \xi(r, \theta)$ (dotted curves; the solid lines denote the poloidal magnetic field/velocity stream lines; the straight dashed line is the Alfvén surface) in a $10^8 r_o \times 10^8 r_o$ region for an ionizing luminosity $L = 3.3 \times 10^{42}$, erg s^{-1} ; this calculation of ξ ignores the reduction of L at large r due to absorption. The values of the corresponding quantities are noted on each dashed curve. The parameters are the same as those of Figure 1. [See electronic edition of the Journal for a color version of this figure.]

There are several points to note about equation (33) and Figure 3b: (i) If distances are scaled by the Schwarzschild radius, r_S , and the accretion rate by its Eddington value, \dot{M}_{Edd} , the ionization parameter, $\xi(r, \theta)$, depends primarily on the normalized accretion rate \dot{m} and $\mathcal{N}(\theta)$; as a result, our analysis and the corresponding ionization structure of the wind, are applicable to accreting black holes of any size. Note that, had one assumed $L \propto \dot{m}$, the expression for ξ would be independent even of \dot{m} ; we believe that this would be in disagreement with observation; (ii) The ionization parameter ξ is much higher near the central engine (e.g. within a few hundreds to thousands Schwarzschild radii) with the wind highly ionized in this region and for a given r it drops precipitously with θ ; (iii) For a given θ , the value of ξ drops with distance (with $\xi \propto 1/r$ for our favorite value of $q \simeq 1$); (iv) ξ increases linearly with increasing accretion rate \dot{m} , implying decreasing source obscuration for high values of \dot{m} as seen in equation (30), in agreement with observation (Tueller et al. 2008); (v) The wind is fully ionized in regions sufficiently close to the central engine thus no contribution to the absorption lines in the spectrum.

One should note that, as written, the expression of equation (33) is a local one, i.e. it does not take into account neither the absorption of the X-ray radiation in its propagation along the LOS wind nor the corresponding re-emission, both of which would modify the local ionizing spectrum, and thus also the global ionization structure shown in Figure 3b here. These effects are small at small values of the radius ($\log x \lesssim 3$ and for relatively hard spectra $\alpha \simeq 1 - 2$), where the ionization of the gas is high and its absorption depth small at all energies; they become more significant at larger radii and they are taken into detailed consideration in our model calculations as discussed below.

It should also be cautioned at this point, that while $\xi(r, \theta)$ is the primary parameter that determines the ionization state of the X-ray illuminated gas, the latter depends also on the spectrum of the incident radiation, as the resulting electron temperature is roughly equal to the mean photon energy of the ionizing radiation. In the calculations presented herein we assume a single power-law with an energy spectrum $L_\nu \propto \nu^{-\alpha}$ between 13.6 eV and 13.6 keV and $\alpha = 1.5$ as a fiducial model (e.g. Sim et al. 2008). More realistic incident spectral distributions (those used, e.g., in Everett 2005; Sim 2005; Schurch & Done 2007) can be easily accommodated within **XSTAR** likely leading to results that are not substantially different from those of the next sections, although we defer such studies to future publications.

2.2.2. Radiative Transfer in the Wind

As noted above, equation (33) is strictly valid when the attenuation of the radiation field by the wind itself is small; it is used in the computation of the ionization state only for the innermost, highly ionized regions of the wind, while at larger radii we use the absorbed radiation field is employing **XSTAR** for the computation of the relevant opacities; the method is described below and it is very similar to the recent work of, e.g., Schurch & Done (2007), Dorodnitsyn, Kallman & Proga (2008) and Schurch, Done & Proga (2009). Since at present we are interested mainly in the absorption properties of the above configuration, whose Thomson opacity is generally small, we treat the gas along the LOS independently as a collection of radially discrete slabs of constant (local) density, and the total column depends only on the LOS angle θ in accordance with Figure 2a. At large distances where the value of the ionization parameter drops and He and H opacities become important, we let **XSTAR** subdivide each zone as necessary for the proper treatment of the radiative transfer; since in this case the absorption mean-free path at the characteristic frequencies is much smaller than the local radius, the plane parallel geometry employed by **XSTAR** for this purpose is adequate.

With the ionizing luminosity L and a spectrum specified at $x = 1$, the entire LOS wind with the radial length scale of $\log(\Delta x) \simeq 10$ is divided up into a number of (plane parallel) slabs/zones (typically ~ 40) of logarithmically-equal thickness in radius; i.e. $\Delta x/x = \text{const.}$

Then, using **XSTAR** we calculate the absorption and emission coefficients within, say, the $(i + 1)$ -th zone, using as input the (properly normalized) output spectrum of the i -th zone, L_i . We thus obtain the forwardly emitted spectrum in emission lines $L_{i+1}^{(\text{line})}$ and in continuum $L_{i+1}^{(\text{cont})}$ by computing the free-free, free-bound and bound-bound atomic transitions within the $(i + 1)$ -th zone (see **XSTAR** manual), while we ignore for this calculation the part of the backward directed flux. We also compute the fraction of the radiation flux of the i -th zone, L_i , that is transmitted through the $(i + 1)$ -th zone, $L_{i+1}^{(\text{tr})}$, given by

$$L_{i+1}^{(\text{tr})} = L_i e^{-\tau(i+1)} , \quad (34)$$

where $\tau_{i+1}(N_{H,i})$ is the optical depth (including continuum and line photoabsorption as well as Thomson scattering) of the $(i + 1)$ -th zone, with $N_{H,i}$ being the total hydrogen equivalent column of this slab. Finally, we produce the (properly normalized) spectrum of the $(i + 1)$ -th zone, by adding the forwardly emitted and transmitted spectra, i.e.

$$L_{i+1} = L_{i+1}^{(\text{tr})} + L_{i+1}^{(\text{cont})} + L_{i+1}^{(\text{line})} , \quad (35)$$

with the process being iterated with L_{i+1} in place of L_i , to compute L_{i+2} and so on.

2.2.3. Modeling Absorption Line Profiles

The above procedure can be applied to a specific atomic transition to produce the resulting line profile and an absorption feature since this is the dominant process along the observer's LOS to the point-like ionizing source. The corresponding emission is distributed isotropically and makes a negligible contribution to specific intensity at the particular frequency. The radiation transfer of a specific feature is dominated by the optical depth of the wind at the specific frequency $\tau(\nu)$, which is expressed by

$$\tau(\nu) = \sigma(\nu) N_H(\nu) , \quad (36)$$

with the line photoabsorption cross-section

$$\sigma = 0.01495 (f_{ij} / \Delta\nu_D) H(a, u) , \quad (37)$$

where f_{ij} is the oscillator strength of the transition between the i -th and j -th levels of an ionic species and $\Delta\nu_D$ is the Doppler broadening factor estimated by $\Delta\nu_D \approx (\Delta v_{\text{turb}}/c)\nu_0$ relative to the centroid (rest-frame) frequency ν_0 with v_{turb} being either thermal or turbulent velocity of the medium, assuming that the overall absorption profiles are well approximated locally by the Voigt function $H(a, u)$ (e.g. Mihalas 1978; Kotani et al. 2000; Hanke et al. 2009). This represents a line profile whose centroid is dominated by the Doppler broadening while the wings are characterized by the damping/Lorentzian profile and defined by

$$H(a, u) \equiv \frac{a}{\pi} \int_{-\infty}^{\infty} \frac{e^{-y^2} dy}{(u - y)^2 + a^2} . \quad (38)$$

In the above expression, we use $a \equiv \Gamma/(4\pi\Delta\nu_D)$ where Γ is the Einstein coefficient and $u \equiv (\nu - \nu_0)/\Delta\nu_D$ is the dimensionless frequency spread about the transition frequency. Irrespective of their thermal or turbulent velocities, the winds we consider provide a well defined velocity shear between two adjacent slabs, whose effect on the radiative transfer of a line photon is very similar to that of the turbulent velocity. To rid the situation of as much unwanted uncertainty as possible we then consider the thermal and turbulent broadenings to be negligible and we consider only the shear broadening, so that

$$\Delta\nu_D \approx (\Delta v_{\text{turb}}/c)\nu_0 = (\Delta v_{\text{sh}}/c)\nu_0 , \quad (39)$$

with Δv_{sh} being the LOS velocity shear. In addition to the broadening, the velocity of the absorbing medium shifts also the transition frequency blueward as $\nu'_0 = \nu_0/[1 - v_{\text{los}}(x, \theta)/c]$ where $v_{\text{los}}(x, \theta) = v_r(x, \theta)$ is the flow velocity along LOS and ν'_0 is the overall observed frequency. With these considerations the expression for the dimensionless frequency spread about the specific transition reads

$$u(x, \theta) = \frac{\nu/\nu_0 - 1/[1 - v_{\text{los}}(x)/c]}{\Delta v_{\text{sh}}/c} . \quad (40)$$

2.2.4. Modeling the Absorption Measure Distribution (AMD)

In a wind model with well-defined density as a function of radius along the LOS, it is natural to use the value of ξ , the parameter that determines the presence (or not) of a given ion, as a proxy for the radius r along the wind in order to study the structure of its ionization. Then the hydrogen equivalent column of specific ions, N_H , as a function of ξ can be used to determine the wind density distribution as a function of radius. This has been precisely the approach of HBK07, who defined the AMD as the hydrogen equivalent ion column density per logarithmic ionization parameter interval; in view of our specific wind models, this has the following dependences [Eqns. (30) and (33)]

$$\text{AMD}(q; \xi) \equiv \frac{d[N_H(r, \theta)]}{d[\log \xi(r, \theta)]} \propto r^{2(q-1)} \propto \xi^{\frac{2(q-1)}{1-2q}} . \quad (41)$$

Therefore, depending on the specific run of the wind density with radius (via q), the AMD is constant, i.e., independent of the radius r or ionization parameter of the plasma ξ when $q = 1$, while it scales as $\text{AMD} \propto r^{-1/2} \propto \xi$, i.e., monotonically increasing with ionization ξ for the BP82 models ($q = 3/4$).

3. Results

In this section we discuss in detail the implementation of the procedures described above and the ensuing results concerning the properties of individual atomic transitions as

well as their dependence on the parameters of the problem. In particular we focus on specific ionic charge states that are important in that they can serve as spectroscopic diagnostics of the ionization state of the wind medium. Because of the specific, continuous decrease of the MHD wind density inherent to the accretion-origin wind scenario, our models span a wide range of ionization parameter space and hence a large number of the corresponding atomic transitions (in absorption). Their global properties are encapsulated in the AMD, namely the distribution of (locally) absorbing column per logarithmic ionization parameter interval, a quantity originally introduced by HBK07, which can and has been compiled for a number of AGNs using comprehensive fits to the ensemble of absorption features in their entire X-ray spectrum (Behar 2009). Furthermore, given that to each ionization state of the plasma corresponds also a specific wind velocity, there exists a correlation between the presence of a specific atomic transition and the corresponding plasma velocity. Employing this generic property, we demonstrate a progressive absorption of the incident X-ray by matter outflowing at the different velocities (as discussed in §2.2), to produce the eventual absorption line profile of specific transitions. Finally, because of the strong dependence of the wind column density along the LOS angle θ , as discussed in §2.1, we consider two representative cases for comparison [employing always the $q = 1$ field geometry and the parameters used in producing Figs 1-3], namely $\theta = 30^\circ$ (high latitude LOS) and 60° (low latitude LOS).

Considering the underlying complexity of the observed broad-band SEDs of AGNs we have decided to adopt the simple prescription of a single power-law form for the ionizing flux discussed above and use different values of its slope α to simulate the diversity of observed AGN SEDs. This approach, while it should be viewed with caution vis-à-vis the detailed properties of the wind ionization, we believe that it is sufficient in capturing the trends of the winds' ionization properties with changes in the overall AGN SED. The photoionization calculations we present include the most important elements (H, He, Ca, Na, O, Ne, Mg, Si and Fe) with abundances set to the solar values (Grevesse, Noels & Sauval 1996). Based on this set-up the major characteristics of our hydromagnetic wind are listed in Table 1 which we shall discuss in subsequent sections.

3.1. Absorption Measure Distribution (AMD)

The unique characteristic of any wind model ionized by a point-source located at its origin is the radial distribution of density and therefore the corresponding distribution of the ionization states of the different elements seen in absorption in the source continuum. A particular wind model is therefore characterized by the distribution of the ionization states of the different elements, their velocities and the distribution of their column densities or their (local) equivalent hydrogen column N_H ; these determine the run of the wind's density

Table 1. Characteristic Wind Properties of Our Models.

| <i>Parameter</i> ^a | <i>Fiducial Value</i> ($\theta = 30^\circ/60^\circ$) | <i>Physical Significance</i> |
|----------------------------------|--|---|
| \hat{M} | 10^6 | Mass of the central black hole in units of M_\odot |
| α | -1.5 | Power-law index of the incident spectrum (in energy) |
| L_X | $3.3 \times 10^{42} \text{ erg s}^{-1}$ | Incident X-ray luminosity |
| r_o | $\sim r_s$ | Radius of the innermost foot point of the wind |
| q | 1 | Scaling of magnetic fields |
| \dot{m} | 0.1 | Dimensionless (conserved) mass-accretion rate |
| η_W | 0.5 | Outflow (wind) rate relative to mass-accretion rate \dot{m} |
| ϵ | 0.2 | Radiative efficiency |
| x_{in} | $6.7/2.0$ | Dimensionless LOS Inner radius of the wind |
| $n(x_{\text{in}})$ | $1.9 \times 10^9/4.5 \times 10^{10} \text{ cm}^{-3}$ | Density of the wind at $x = x_{\text{in}}$ |
| Δx | $\sim 10^{10}$ | LOS length scale of wind |
| $\log \xi(x_{\text{in}})$ | $8.62 / 8.3$ | Ionization parameter at $x = x_{\text{in}}$ |
| $v_{\text{los}}(\text{Fe XVII})$ | $\sim 100 - 300 \text{ km s}^{-1}$ | Characteristic LOS velocity of Fe XVII |
| $\log \xi(\text{Fe XVII})$ | $\sim 2.2 - 3$ | Ionization parameter of Fe XVII |
| $\log x(\text{Fe XVII})$ | $\sim 6 - 7/5 - 6$ | LOS distance of Fe XVII |
| $v_{\text{los}}(\text{Fe XXV})$ | $\sim 2,000 - 4,000/1,000 - 3,000 \text{ km s}^{-1}$ | Characteristic LOS velocity of Fe XXV |
| $\log \xi(\text{Fe XXV})$ | $\sim 4 - 5$ | Ionization parameter of Fe XXV |
| $\log x(\text{Fe XXV})$ | $\sim 4 - 5/3 - 4$ | LOS distance of Fe XXV |
| $v_{\text{los}}(\text{O VII})$ | $\sim 40 - 150 \text{ km s}^{-1}$ | Characteristic LOS velocity of O VII |
| $v_{\text{los}}(\text{O VIII})$ | $\sim 100 - 600/100 - 300 \text{ km s}^{-1}$ | Characteristic LOS velocity of O VIII |
| ΔN_H | $\sim 2.6 \times 10^{21}/1.8 \times 10^{22} \text{ cm}^{-2}$ | Local wind column density per slab |
| N_H | $\sim 3.9 \times 10^{22}/2.5 \times 10^{23} \text{ cm}^{-2}$ | Integrated wind column density over $-1 \lesssim \log \xi \lesssim 4$ |

^a See the text for the template parameter values in detail.

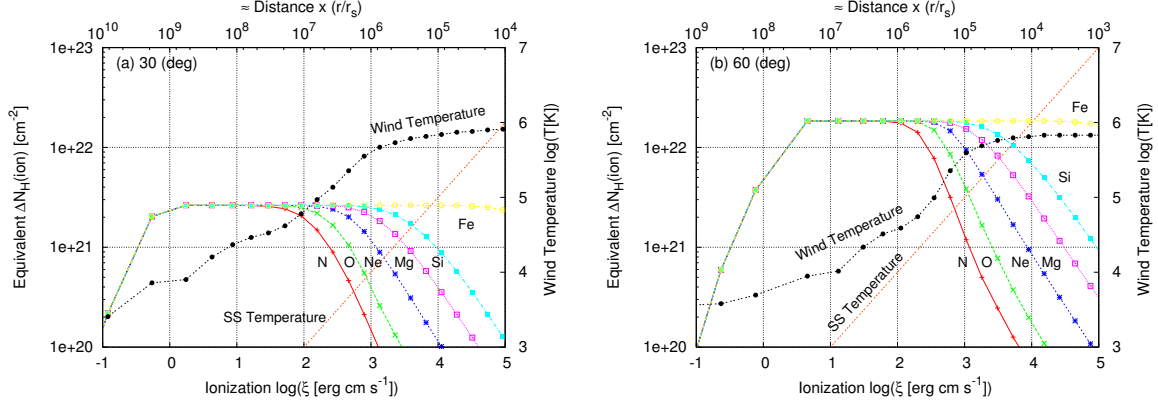


Fig. 4.— Simulated hydrogen-equivalent (local) column density (per slab) $\Delta N_H(\text{ion})$ for major ionic elements (N, O, Ne, Mg, Si and Fe) and wind temperature T (right axis) in the fiducial model for (a) 30° and (b) 60° . Analytic self-similar (SS) wind temperature is also shown. Corresponding LOS (normalized) distance $x(\equiv r/r_s)$ is also shown in the upper axis. The parameters are the same as in Figure 1. Rapid decrease of ΔN_H in the highest (lowest) end of ξ is due to fully stripped ions (neutral ions). [See the electronic edition of the *Journal* for a color version of this figure.]

and velocity with the radius r . For example, in the accelerating phase of a spherical wind, both the ionization parameter and the velocity increase with distance and “freeze” once it has achieved its terminal velocity, while the column density of ions decreases faster than $1/r$ if an ion is present in the wind accelerating stage, leveling off to $N_H \propto 1/r$ once terminal velocity is achieved.

The characteristic properties of the winds presented in §2 are drastically different from those of spherical winds. In particular: (i) The ionization parameter ξ and the corresponding LOS velocity v_{los} decrease with distance as r^{-1} and $r^{-1/2}$ respectively to encompass a large number of ionization states of many elements at different velocities. (ii) The specific column density per decade of radius translates for any element to a (local) equivalent hydrogen column ΔN_H that is independent of the radius r .

For a given wind model and ionizing spectrum, one can produce the corresponding AMD profiles, i.e. the global distribution of its ionization properties which can then be compared to observations. We do so in this section and compare the results to the recent AMD analysis of IRAS 13349+2438 observations (HBK07). The results of our calculations are shown in Figure 4 where we present the AMD for the $q = 1$ wind models, with the ΔN_H plotted as a function of $\log \xi$ for $\theta = 30^\circ$ in (a) and 60° in (b). Also superimposed is the plasma (gas) temperature $\log T$ computed by **XSTAR** under local thermal equilibrium conditions along with the analytic self-similar (SS) temperature ($\propto 1/r$). The ionized wind

temperature decreases monotonically from $T \sim 10^6$ K down to $T \sim 10^{3.5}$ K as ξ decreases from $\log \xi \simeq 5$ to $\log \xi \simeq -1$ a range relevant to the observable ionic states of the major elements. For reference, the corresponding (dimensionless) LOS distance $x \equiv r/r_S$ from the central engine is also shown in the upper x-axis where in this run $r_S \cong 3 \times 10^{11}$ cm. As seen, the local column densities of the irradiated ions (shown here are the six major elements: N, O, Ne, Mg, Si and Fe) are found to be all distributed at constant value of ΔN_H over many decades of ξ (and therefore a similar range in LOS distance too), namely $\Delta N_H \sim 2.6 \times 10^{21}$ cm $^{-2}$ for 30° and $\sim 1.8 \times 10^{22}$ cm $^{-2}$ for 60° , reflecting the different wind density at these different LOS (see Fig. 2a). This results in an integrated column of $N_H \sim 3.9 \times 10^{22}$ cm $^{-2}$ for 30° and $\sim 2.5 \times 10^{23}$ cm $^{-2}$ for 60° over $-1 \lesssim \log \xi \lesssim 4$. The constant value of AMD is a unique characteristic of the $q = 1$ models with the value corresponding to case (a) ($\theta = 30^\circ$) in good agreement with the observed AMD of IRAS 13349+2438 analyzed by HBK07.

As shown here, the computed temperature has a radial dependence (gradient) close to the desired $1/x$ one for $x \gtrsim 10^5$, but it is constant for $x \lesssim 10^5$. However, because the thermal pressure is smaller than the wind ram pressure over the entire domain, the thermal pressure effects on the wind density profiles are not significant. We have also compared the heating/cooling time scales of **XSTAR** and were found to be shorter than the local dynamical time scale r/v , indicating that the temperature distributions of Figure 4 are indeed correct, even though not dynamically important. We have obtained by another calculation a wind solution similar to Figure 4 in the cold-flow limit ($K = 0$).

It should be noted that the decrease of ΔN_H at high values of ξ is due to the fact that **XSTAR** by default does not provide the column density of fully ionized (bare) ions. This apparent decrease is just due to the fact that all considered elements become progressively (completely) ionized at high ξ values. At the other end of the plot, i.e. for small values of ξ , ΔN_H appears to decrease too because the wind becomes too cold (gas temperature of $T \lesssim 10^{3.5}$ K) to participate in radiative processes, i.e. each species turns neutral, an ionization state also not included in the calculation of the hydrogen equivalent column. The calculated AMD is otherwise constant, as expected. The fact that the corresponding ΔN_H is the same in this regime irrespective of the elements used in the computation is a testimony that our models implement **XSTAR** correctly, so that the sum of the abundances of all ions of any element, when corrected for the elemental abundance, yields the same value of ΔN_H . We also see that the (relatively) lighter elements (say, oxygen) become fully ionized at lower ξ than heavier ones (say, iron), also as expected. In essence, the overall trend of the model AMD in both LOS cases (a) and (b) appears to be very similar to one another (i.e. constant value of ΔN_H independent of ionization state) except for the fact that the local column ΔN_H for 30° in (a) is about a factor of ~ 10 lower than that for 60° in (b) because of the angular dependence of the wind density function $\mathcal{N}(\theta)$ (also see Fig. 2a).

It is also of interest to show the differential form of Figure 4, i.e. the columns of specific charge states of a given ionic element ΔN_{ion} . This is shown in Figure 5 for iron again

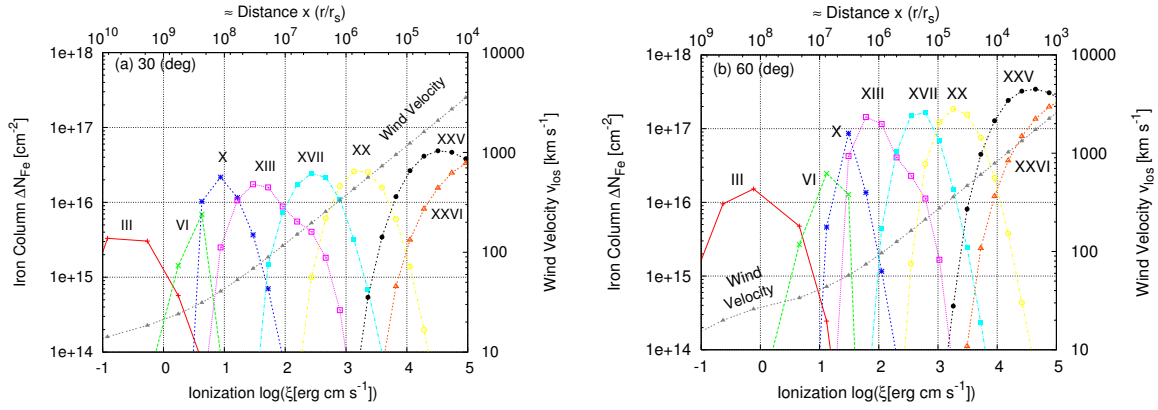


Fig. 5.— Simulated local iron column density ΔN_{Fe} distribution for various iron charge levels (Fe III, Fe VI, Fe X, Fe XIII, Fe XVII, Fe XX, Fe XXV, and Fe XXVI) and LOS velocities v_{los} (right axis) for (a) 30° and (b) 60° with the same fiducial model parameters as in Figure 4. [See the electronic edition of the Journal for a color version of this figure.]

for two different LOS. This figure shows the emergence of various ionization states of iron (shown here are Fe III, Fe VI, Fe X, Fe XIII, Fe XVII, Fe XX, Fe XXV and Fe XXVI) along with the corresponding LOS velocity v_{los} for $\theta = 30^\circ$ in (a) and 60° in (b) corresponding to Figure 4. As discussed above, the higher ionization states are present at the inner sections of the wind (smaller x), being replaced by lower ionization ions at larger radii with their columns given in absolute values ΔN_{Fe} instead of the hydrogen-equivalent values ΔN_H . One should note that the maximum value (peak) of ΔN_{Fe} for a specific charge state is approximately constant until one gets to the lowest ionization states, located at the largest distances (see, e.g., Murray & Chiang 1998, for a similar transition) because the fraction of neutral iron relative to the total iron starts increasing as mentioned earlier for Figure 4. Of interest is also the LOS wind velocity v_{los} that corresponds to a given value of ξ . While v_{los} decreases like $\propto \xi^{1/2}$ at high values of ξ (as $\xi \propto r^{-1}$ and $v_{\text{los}} \propto r^{-1/2}$), it deviates from this dependence at the largest radii because of the additional reduction of the X-ray flux due to absorption. The velocity at which each ion has its maximum column and the range in v_{los} over which it has substantial column are of interest because they determine the absorption line profile of the specific ion. Thus, in the case of (a) $\theta = 30^\circ$, higher charge states such as Fe XXV are found to be blueshifted by a relatively high outflow velocity, $v_{\text{los}} \sim 2,000 - 4,000 \text{ km s}^{-1}$ at $\log \xi \sim 4 - 5$ ($\log x \sim 3 - 4$) while lower charge states such as Fe XVII are blueshifted by only $v_{\text{los}} \sim 100 - 300 \text{ km s}^{-1}$ at $\log \xi \sim 2.2 - 3$ ($\log x \sim 6 - 7$). We emphasize that the latter (Fe XVII) line velocity and column density are also in good agreement with those of IRAS 13349+2438 (HBK07). For $\theta = 60^\circ$ in comparison, the column density increases ~ 10 times but the corresponding line velocity and ionization stage remains roughly the same (but at smaller distances) because both the poloidal velocity and its projection to the LOS are smaller at lower latitudes (see Fig. 2b).

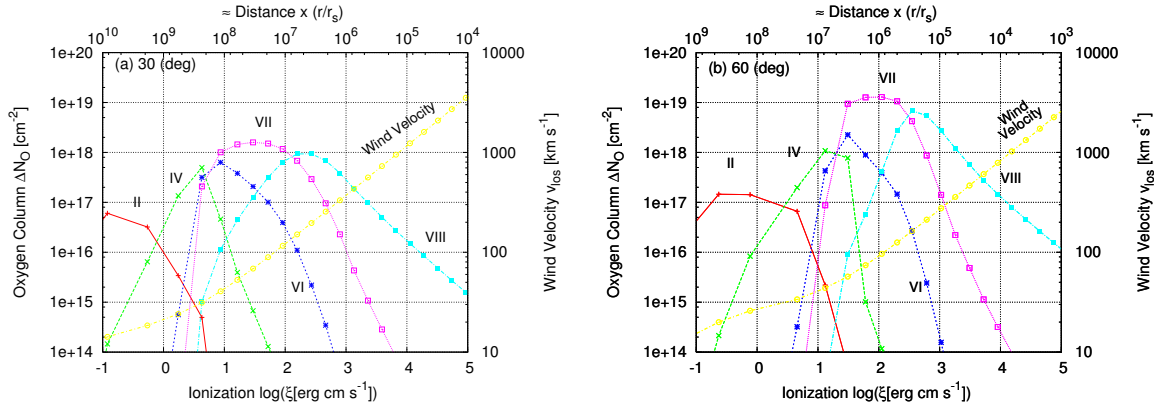


Fig. 6.— Same as Figure 5 but for oxygen. [See the electronic edition of the Journal for a color version of this figure.]

To conclude this section, we show in Figure 6 the column densities of specific charge states of oxygen again for two different LOS at (a) $\theta = 30^\circ$ and (b) $\theta = 60^\circ$, along with the corresponding velocities overplotted as in Figure 5. As expected the corresponding outflow velocities are smaller for O VII ($v \sim 40 - 150 \text{ km s}^{-1}$ at $\log \xi \sim 1 - 2$ or $\log x \sim 7 - 8$) and larger O VIII ($v \sim 100 - 600 \text{ km s}^{-1}$ at $\log \xi \sim 6 - 7$ or $\log x \sim 2 - 3$) for (a) $\theta = 30^\circ$, while similarly for (b) 60° we find $v \sim 40 - 150 \text{ km s}^{-1}$ at $\log \xi \sim 2$ ($\log x \sim 6$) for O VII and $v \sim 100 - 300 \text{ km s}^{-1}$ at $\log \xi \sim 2.5 - 3$ ($\log x \sim 5 - 5.5$) for O VIII, with the former having lower column per ion than the latter, as expected.

One should note that the precise correlations between the wind variables and the observables (i.e. $\Delta N_{\text{ion}}, v_{\text{los}}$) in the present model are primarily a function of the specified mass-accretion rate \dot{m} and LOS angle θ as well as the incident X-ray spectral index α and therefore the model has the freedom to alter the resulting AMD distributions depending on the intrinsic properties of AGNs (here we focused on IRAS 13349+2438 as a case study).

3.2. Absorption Line Spectra

As discussed in the previous subsection and exhibited plainly in Figures 5 and 6, specific charge states of the different elements are present at different values of ξ to which correspond different values of column density and velocity. We have also indicated that the simplest assumption about the optical depth of a specific transition is that it is determined by the velocity shear of the wind, a quantity that is also calculable within our models [see equation (37)]. Armed with this information we present in this section the profiles of specific atomic transitions in absorption. With the spectral emissivity and velocity given, we are also in a position to calculate the corresponding emission profiles. However, since the

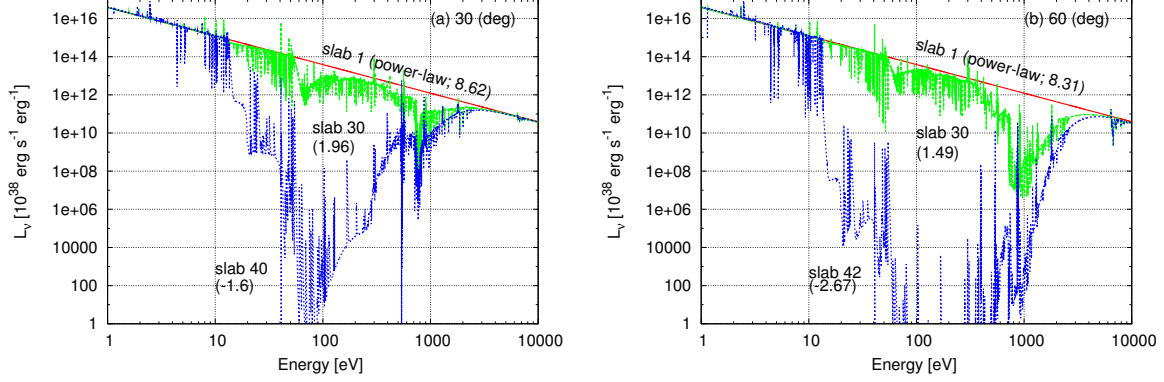


Fig. 7.— Simulated broad-band X-ray spectra L_ν for (a) 30° and (b) 60° as a sequence of progressive X-ray illumination: an initial power-law (slab 1) and the subsequent spectra (as indicated by ionization parameter $\log \xi$ -value of each slab) with the same fiducial model parameter as in Figure 4. [See the electronic edition of the Journal for a color version of this figure.]

most prominent AGN lines lie in the O-UV part of the spectrum, a comprehensive approach would require also a more precise model of the UV part of the spectrum; as such we defer line emission to a future work.

A demonstration of the progressive effect of absorption on the transmitted spectra is presented in Figure 7. This figure exhibits the spectra between 1 eV and 10 keV of the radiation transmitted past the innermost slab 1 (power-law) through the subsequent slabs indicated by the values of $\log \xi$ for two different LOS angles, (a) $\theta = 30^\circ$ and (b) 60° . Absorption by the consistently ionized wind becomes apparent first at energies $E \lesssim 1$ keV, becoming progressively deeper and shifting to lower energies as the radiation propagates through larger wind column. Absorption also increases with the inclination angle θ as one would qualitatively expect. Note that in this simplistic model the incident radiation includes only the X-ray power-law continuum ignoring all the other (potentially rather important) components. Also, it ignores emission that eventually may come into our LOS due to reflection and scattering in the wind. For this reason, the deep absorption imprinted in Figure 7 should not be interpreted literally in a quantitative sense, but as a qualitative indicator of the absorption as a function of ξ along a given LOS.

Let us turn our attention to specific atomic transitions, namely those of Fe XVII and Fe XXV of column ΔN_{Fe} with velocity v_{los} as a function of ξ as given in Figure 5 and shear given by our model. Using the expressions for the photoionization cross-section and Voigt function [eqns. (36)- (38)] one can construct the characteristic absorption profiles; these include both the Doppler blueshift due to LOS velocity v_{los} and the line broadening of the

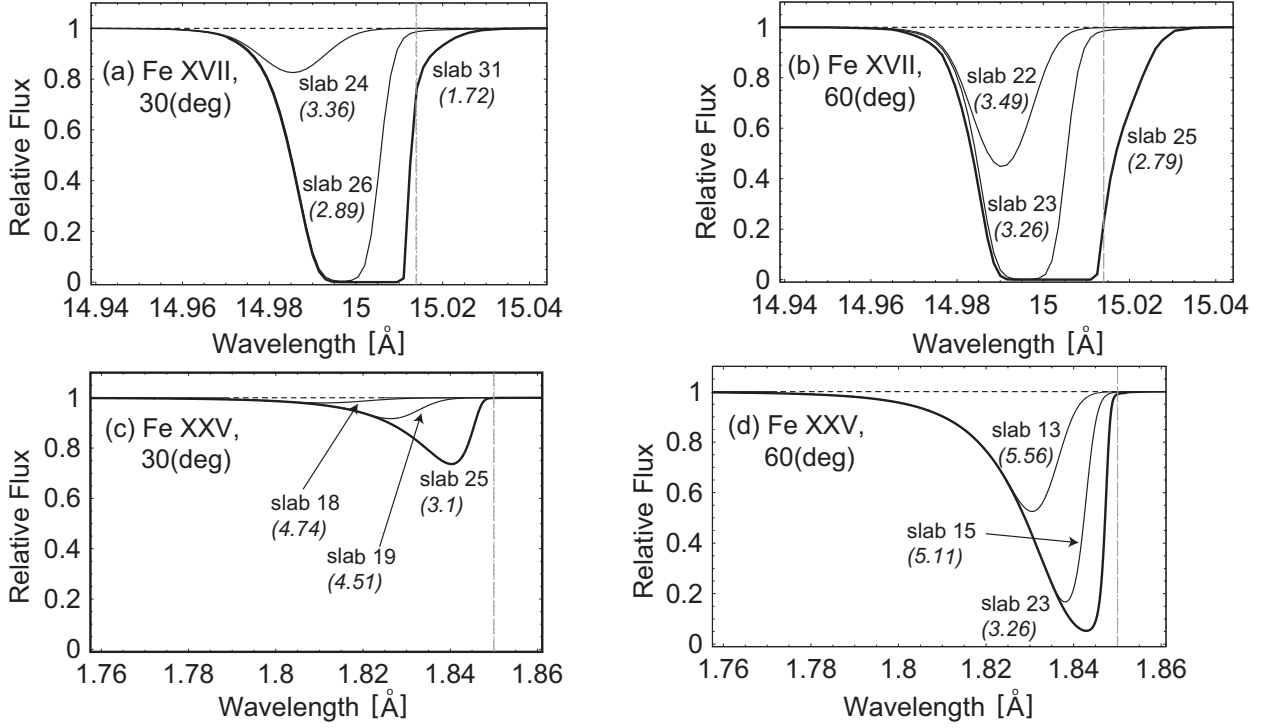


Fig. 8.— A sequence of the simulated absorption features (indicated by ionization parameter $\log \xi$ -value of each slab) for Fe XVII (upper panels) and Fe XXV (lower panels) as the incident X-ray (power-law shown by dotted horizontal lines) transmits through the LOS wind of 30° (left panels) and 60° (right panels) with the same fiducial model parameters as in Figure 4. Vertical dashed lines denote the rest-frame wavelength.

Voigt function in equation (38). Figure 8 shows a sequence of the simulated absorption line for Fe XVII with the rest-frame wavelength at 15.014\AA (upper panels) and Fe XXV with the rest-frame wavelength at 1.850\AA (lower panels) for two LOS angles, $\theta = 30^\circ$ (left panels) and 60° (right panels). We focus here on these prominent iron charge states because they are less contaminated by other adjacent spectral features. We adopted the following values for the relevant atomic data: $f_{ij} = 0.69/2.3$ and $\Gamma = 4.48 \times 10^{14}/2.27 \times 10^{13} \text{ s}^{-1}$ for Fe XXV/Fe XVII, respectively. The figure provides the spectra transmitted through increasing wind column along the LOS. The absorption line obtains its largest blueshift and broadest contribution by ions at the higher values of ξ , becoming progressively deeper, less blue-shifted and narrower as the contribution to the absorption is affected by regions of lower ξ (larger r) which provide the highest column of the specific ion (and also smaller velocities and shear). Again, the spectra are broader and deeper for the higher LOS angles reflecting higher (local) velocities at specific values of ξ and higher overall columns.

In concluding this section we would like to point out the work of Gabel et al. (2003)

on the UV absorption features of NGC 3783 which were found to have velocity structure in agreement with that of the corresponding X-ray ones, thereby arguing for the consistency of the entire wind structure. Also, Collinge et al. (2001) have found that the low ionization Fe absorption features of NGC 4051 had corresponding UV absorption features, while the high ionization, higher velocity X-ray absorption features of the spectrum lacked an equivalent UV absorption, indicating the absence of these ions in the higher ionization, higher velocity plasma.

4. Summary and Discussion

In this work we have presented a detailed study of the ionization structure of model MHD winds off accretion disks; this is our first attempt to model within this context the recent observations of absorption features in the *ASCA*, *XMM* and *Chandra* X-ray spectra, the so-called warm absorbers. To this end we have employed the self-similar 2D hydromagnetic wind models developed by CL94 that provide the fluid 2D density and velocity fields, which we coupled to photoionization calculations using *XSTAR*. Our consideration of magnetocentrifugal (MHD) winds/outflows in this work has been motivated and supported in part by recent observational implications that at least in a number of AGNs and GBHCs the inferred driving mechanism of the observed X-ray ionized wind medium is magnetic rather than thermal or radiative (e.g., see Miller et al. 2006, 2008 for GRO J1655-40; Kraemer et al. 2005 and Crenshaw & Kraemer 2007 for NGC 4151).

Given the scope of our paper, our model wind is necessarily overly simple. It ignores a host of issues that affect the structure of winds off accretion disks and replaces them with the self-similar models of CL94. The interested reader can get a feeling of the multitude and complexity of the issues not addressed in the present treatment by looking at the works of, e.g., Proga (2003) and Proga & Kallman (2004) (and references therein) and also Ohsuga (2009, for disks with several distinct values of the accretion rate \dot{m}). These include, among others, the radiative transfer in the wind, the ensuing effects of radiation pressure and also the influence of the vertical gradient of B_ϕ^2 in the launching of the wind. As shown in these references the winds can be radiation driven in the inner part of the disk (due to the increased flux at this spatial domain) while being magnetically launched at larger radii. In this respect our model winds are quite different in structure and variability from the more realistic winds of Proga (2003) at small radii, while they should be more similar to those of his at larger radii where radiation pressure is smaller and the wind is magnetically launched. Realistic models must by necessity consider the transition of the underlying disk from radiation pressure, at small r , to gas pressure dominance at larger radii; this fact would likely force a different choice of our boundary condition $\psi'(90^\circ)$ and therefore yield a field geometry that breaks the self-similarity of our solutions. Wind models very similar to those used herein but with the

inclusion of the effects of the radiation pressure that break the self-similarity were discussed by KK94 and Everett (2005).

One should therefore view our models with the above caveats in mind. The significance and assumptions of the models we propose is basically justified *a posteriori* by their ability to interpret the observations. Self-similarity is one of the fundamental assumptions of our model winds. However, whether exactly self-similar or not, any model that would attempt to account the entire range of ionic species shown e.g. in Behar (2009) must by necessity cover a very broad range in the photoionization parameter ξ . Then, the column of each such ion provides a measure of the corresponding hydrogen equivalent column N_H as a function of ξ , i.e. the AMD. These two quantities (N_H, ξ) can then be employed to provide a measure of the gas density $n(r)$ as a function of the distance r from the X-ray source. Barring the possibility of several independent regions at different distances but similar columns as indicated by the functional form of the AMD (one could consider this is possibility at the risk of introducing an inordinate number of free parameters), models with radial density profiles as those considered here are a natural consequence of the AMD obtained by the *Chandra* observations.

The wind ionization structure was followed in 1D as described in §2.2, namely along the observer’s LOS, assuming the ionizing source to be point-like. Clearly, a more comprehensive treatment of this problem should take into account also the backward emitted radiation which will reach the observer from the regions of the disk on the other side of the black hole, as well as the scattered radiation, whose effects could be significant. We plan to return to these issues in a future publication.

The 2D structure of the winds considered in our analysis implies, at a minimum, a two-parameter description of the absorption features. However, the self-similarity of the problem simplifies further the treatment by allowing the separation of the r and θ variables with the wind density obtaining the form $n(r, \theta) \propto r^{2q-3} \mathcal{N}(\theta)$. The parameter q is a most important parameter of these models because it determines both the radial dependence of the ionization parameter ξ and the wind column density per decade of radius along a given direction (LOS). In the models examined in the present work we restricted our study to the value $q = 1$, which leads to a radial density profile $n(r) \propto 1/r$. This is an interesting profile in that it provides for an ionization parameter ξ with a similar dependence, i.e. $\xi \propto 1/r$, and most importantly, with equal column per decade in radius, across the entire range in radius and the corresponding range in ξ ; as a result, ionic species of very different ionization properties, existing over a wide range of ionization parameter (and radius), have roughly comparable column densities, independent of the distance and are therefore possible to detect. As noted in CL94, the value of q determines also the axial current distribution in radius within the wind, with the corresponding magnetic energy per unit length at the wind base being also constant per (cylindrical) decade in radius. It is worth comparing our work with that of KK94, who used the same type of MHD wind with the value of q as we do

herein: while these authors focused their study on the effects of dust on radiation transfer, we focus our attention on the effects of the ionizing radiation on the X-ray spectra of AGNs, in particular on the ionized absorbers. KK94 also noted in passing the relevance of their models to the X-ray AGN spectra well ahead of the detailed outflow observations made with *Chandra*.

While the structure of the wind in r and θ is provided by the models of CL94, for the remaining parameters of our models, namely the normalization of the wind density and the X-ray luminosity of the ionizing source we have chosen to use the scalings of ADAFs, or better ADIOS; as a result the X-ray luminosity is proportional to the square of the (normalized) accretion rate at the inner edge of the disk \dot{m}^2 rather than simply \dot{m} , assumed in standard accretion disks. Therefore, restricting ourselves to models with $q = 1$, the global ionization structure of a given wind, including the normalization of the column density, depends only on *two parameters*, namely \dot{m} and the observer’s inclination angle θ . This parametrization provides an extremely economical set of assumptions concerning not only the outflows, i.e. the wind ionization structure seen in absorption in detailed X-ray spectra, but also for the entire (radio-quiet) AGN unification picture: Figure 2 which exhibits the normalization of the wind density as a function of θ along the magnetic field line of $\Psi = \Psi_0$, makes apparent the difference in column between face-on and edge-on views, implying that the wind, if extending to sufficiently large radii, can in fact serve as the proposed molecular torus associated with AGN unification, a point originally made by KK94, also for winds with $q = 1$; it is of interest to note that the few objects for which sufficiently detailed observations exit are consistent values $q \simeq 1$ (HBK07; Behar 2009). Within this same context and ionizing luminosity considerations, one should note the dependence of source obscuration on the X-ray luminosity, namely its reduced value for objects accreting at a higher fraction of their Eddington rate \dot{m} , which apparently is in general agreement with observations. It remains to be seen whether these notions can withstand the scrutiny of more consistent and encompassing observational tests.

At this point we would like to stress the importance of the AMD in the study of AGN outflows/winds, a quantity enunciated by HBK07 and modeled in detail in the preceding sections. Analyses similar to those of HBK07 and Behar (2009) are indispensable because they produce a consistent analysis of the entire set of absorption features in the AGN X-ray absorption spectra. At the same time they underscore the unique value of X-ray spectroscopy which, in a wavelength band of ~ 1.5 decades, can encapsulate the properties of ions that span ~ 5 orders of magnitude in ionization parameter and, for models with $q \simeq 1$, a similar range in radius; at the same time, measurement of their absorption columns yields the equivalent hydrogen column of the flow, N_H , over a similar range in radius, thereby going a long way toward the determination of the physics underlying the outflow dynamics. The fact that the AMD analyses to date are roughly independent of ξ provide support to our use of the $q = 1$ or $n(r) \propto 1/r$ models, reiterating that a similar density profile was invoked

on the basis of AGN and GBHC timing properties (Papadakis, Nandra & Kazanas 2001; Kazanas, Hua & Titarchuk 1996).

We have thus presented a concrete example of the AMD dependence on ξ for our $q = 1$ models with $\epsilon = 0.2$, $\dot{m} = 0.1$ and two different values of the observer’s inclination angle (see table 1 for details). As expected we found the AMD to be constant, i.e. independent of ξ , over many decades in this parameter (i.e. the local column density ΔN_H is independent of ionization states ξ of ions). With $\dot{m} = 0.1$, $\eta_W \simeq 0.5$, equation (30) implies $\Delta N_H \sim 2.6 \times 10^{21} \text{ cm}^{-2}$ (yielding a total column of $N_H \sim 3.9 \times 10^{22} \text{ cm}^{-2}$) for $\theta = 30^\circ$ and $\Delta N_H \sim 1.8 \times 10^{22} \text{ cm}^{-2}$ (total of $N_H \sim 2.5 \times 10^{23} \text{ cm}^{-2}$) for 60° over $-1 \lesssim \log \xi \lesssim 4 \text{ erg cm s}^{-1}$, in good agreement with the observed AMD of IRAS 13349+2438 (HBK07; Behar 2009) and also some other AGNs detailed below. One should note that these values depend primarily on \dot{m} and θ and are independent of the black hole mass. The mass of the object gets involved only as a measure of its total luminosity, which does not appear in the expression for N_H , implying that these models could in principle be applicable also in GBHCs. High quality X-ray absorption data are in fact available for the GBHC GRO J1655-40 and were used to argue for magnetic driving of the wind in this system too (Miller et al. 2006, 2008). These spectra are distinguished from those of AGNs by the prominent absence of low ionization state ions. This is to be expected given that the presence of the companion star limits the extent of the disk to roughly half the distance between the two objects or $r \simeq 10^{12} \text{ cm}$. Given that the Schwarzschild radius of the compact object is $r_S \simeq 10^6 \text{ cm}$ the entire disk size covers only a range of $\log x \sim 6$ in radius; considering (based on Fig. 4) that in the inner region of the wind ($r \sim 1000 - 3000 r_S \sim 10^9 \text{ cm}$) major elements (even heavier species) are almost fully ionized, one would expect the presence of ions over only a factor of 1000 in ξ , in rough agreement with the observation.

Given that our models provide also the complete velocity field of the MHD wind we have also produced a sequence of synthetic absorption profiles as described in §2.2 and shown in §3.2. We have done so for two charge levels of Fe, namely Fe XXV and Fe XVII. With our fiducial model predicting the Fe XVII column to be maximum at $\log \xi \sim 2.2 - 3 \text{ erg cm s}^{-1}$, we then infer the corresponding LOS velocity (see Fig. 5) to be $v_{\text{los}} \sim 100 - 300 \text{ km s}^{-1}$ in excellent agreement with the observed values of IRAS 13349+2438. It is important to note that the model produces not only the correct velocity v_{los} at the maximum value of $\Delta N_{\text{Fe}}(\xi)$ but also the observed $\Delta N_H(\xi)$ normalization *for the same inclination angle*. It is therefore possible with measurements of the combined line widths and column densities to reproduce within the present models both q , θ and \dot{m} , thereby providing a complete specification of these winds. In addition to IRAS 13349+2438, the nearby bright Seyfert MCG 6-30-15 has been observed to show, as one of the multiple ionization zones, an X-ray ionized absorber with an outflow velocity of $\sim 1900 \text{ km s}^{-1}$ at $\log \xi \sim 3.85$ and $N_H \simeq 9 \times 10^{22} \text{ cm}^{-2}$ (e.g. Young et al. 2005; Holczer, Behar & Arav 2009) also in good agreement with our model results for $\dot{m} \sim 0.1$ (see Fig. 5). Clearly, a different choice of a set of conserved quantities

(wind variables) in the model would produce a slightly different field line geometry in which the resulting MHD outflow could in principle obtain higher LOS velocities (perhaps by factors of magnitudes), and this will be studied in detail in a future work.

As noted above our model is quite successful in reproducing the observed AMD of IRAS 13349+2438. More recently, Behar (2009) presented a compilation of the AMD of a number of AGN with $dN_H/d\log\xi$ which are slightly different from constant but with q -values of $n(r) \propto r^{2q-3}$ which are still very close to unity; e.g. NGC 3783 ($q \sim 0.89$), NGC 5548 ($q \sim 0.94$), NGC 7469 ($q \sim 0.9$) and MCG-6-30-15 ($q \sim 0.95$). We believe some of these AMDs are sufficiently close to those of our fiducial model to be virtually indistinguishable. By comparison, the MHD wind models of BP82 have $q = 0.75$ and $n(r) \propto r^{-3/2}$. Their ionization parameter decreases more slowly with r ($\xi \propto r^{-1/2}$) and hence a range of 5-6 decades in ξ implies a range of 10-12 decades in radius with the corresponding distances being unrealistic. Most importantly, the wind columns would decrease with radius ($N_H \propto r^{-1/2}$) and the AMD dependence on ξ would be $dN_H/d\log\xi \propto \xi$, in clear disagreement with these observations, and thus their model is essentially ruled out (Behar 2009).

Despite the apparent success of this first model, one should bear in mind that several aspects have been treated in a rather simplified fashion. Here we discuss some of them and their influence on the results presented so far:

1. The shape of the ionizing spectrum used so far ($F_\nu \propto \nu^{-\alpha}$ between 13.6 eV and 13.6 keV with $\alpha = 1.5$) is quite simplistic, however, such spectra are often used in similar type calculations (e.g. Sim et al. 2008). This is a crude approximation to the observed spectra characterized by complex spectral shapes. Spectral features like the BBB and the UV to X-ray luminosity ratio α_{OX} (Elvis 2000) play a role in our results (a recent review of the broad band AGN SEDs can be found, e.g., in Risaliti & Elvis 2004). More recently, Grupe et al. (2004) sampled 110 bright soft-X-ray selected AGNs for a simultaneous study of Optical/UV and X-ray data and reported strong correlations between the X-ray spectral slope and the Optical/UV slope which should be included in a more comprehensive treatment. Multi-components of the broad-band AGN spectra, as those discussed by Elvis (2000) and Risaliti & Elvis (2004), should play an important role in characterizing the observed X-ray spectral features. Adding softer photons (responsible for the Optical/UV components) could impact the radiative transfer between those more complex photon distributions and the ionized matter (see, e.g., Everett 2005; Sim 2005, for multi-component injected spectra). In fact, we have mimicked the presence of such softer photons by choosing larger values of the spectral index of our models ($\alpha \gtrsim 2$). For the same total luminosity (implemented in the definition of ξ), it was found in this trial run that the radial position of the peak column density of a given ion (e.g. Fe XVII) decreases, because the presence of a given ion requires a certain flux of *ionizing* photons per atom; in a steep spectrum the proper ratio is found at larger values of the parameter ξ or correspondingly smaller values of the distance $x = r/r_S$. As a result, the widths of the corresponding transitions should be larger and therefore the proper

ionizing spectrum is necessary for the correct interpretation of the relations between ionic column densities and wind kinematics (see Everett 2005; Sim 2005, for a similar approach).

2. The ionizing source has been considered, for simplicity, to be point-like. A source of finite size will provide for more complex illumination, especially for parts of the wind at which the source angular extent is significant. Most importantly an extended source would impact the absorption line profiles, since a line of sight may pass through matter other than that used in section 3.2. Finally, to treat the radiative transfer correctly at all energies, one should eventually need to resort to a 2D approach rather than the 1D model (radial only) presently used, which would modify the global ionization structure (Fig. 3b).

3. The wind equations, as presently implemented include only MHD forces, while it is apparent that in the presence of the ionic species we produce one should also include the effects of radiation pressure. Because the latter depends on the ionization state of the plasma which in turn depends on its kinematics, implemented correctly, this should be done iteratively in a way similar to Everett (2005). Based on the rather small effect that the radiation force seems to have on the structure of these winds, we believe that our present results are generally valid.

In summary, we have presented above a first attempt at interfacing theoretical models of MHD winds with AGN observations, in particular the absorption features in their X-ray spectra of ionized outflows. We have placed most of our emphasis on modeling the corresponding AMDs, which, based on the existing observations seems to favor a specific value of the model parameter q which determines the radial density dependence of our models, namely $q \simeq 1$. With the value of this parameter set by observation, our models present a *two-parameter* family of AGN wind structure, namely \dot{m} and θ . We have found that, based on the limited number of objects discussed above, our models fare rather well in accommodating the observations and the possibility of incorporating AGN unification within the same models, as discussed in KK94. There is still a multitude of issues related to X-ray absorption that remain open, e.g. whether the model can accommodate the high velocity ($v/c \sim 0.1 - 0.25$) outflows associated with X-ray absorption features (see, e.g., Sim 2005; Sim et al. 2008, for some attempts with Monte Carlo simulations) in the spectra of some bright quasars such as APM 08279+5255, PG 1211+143 and PDS 456 (e.g. Chartas et al. 2009; Pounds & Reeves 2009; Reeves et al. 2009). In the context of our model this point may be well explained with an optimized magnetic field geometry [i.e. $\Psi(r, \theta)$ distribution determined by GS-equation (27)] that provides a favorable LOS velocity component. Important as they are, these go beyond the scope of the present work and we expect to return to them in future publications.

We are grateful to our anonymous referee for his/her constructive comments that improved the manuscript. We would like to thank Tim Kallman for his help with XSTAR

incisive comments. We express our gratitude to George Chartas for his comments on the model, Takanori Sakamoto and Javier Garcia for their assistance with scripting and running XSTAR as well as helpful comments. This work was supported in part by NASA ADP grant.

REFERENCES

- Antonucci, R. R. J. & Miller, J. S. 1995, *ApJ*, 297, 621
- Behar, E. et al. 2003, *ApJ*, 598, 232
- Behar, E., 2009, *ApJ*, 703, 1346
- Boroson, T. A. 2002, *ApJ*, 565, 78
- Boroson, T. A. & Green, R. F. 1992, *ApJS*, 80, 109
- Blandford, R. D & Payne, D. G. 1982, *MNRAS*, 199, 883 (BP82)
- Blandford, R. D & Begelman, M. C. 1999, *MNRAS*, 303, L1
- Brandt, W. N., Chartas, G., Gallagher, S. C., Gibson, R. R., & Miller, B. P. 2009, [arXiv:0909.0958v1](https://arxiv.org/abs/0909.0958v1)
- Chartas, G., Saez, C., Brandt, W. N., Giustini, M., & Garmire, G. P. 2009, *ApJ*, 706, 644
- Contopoulos, J., & Lovelace, R. V. E. 1994, *ApJ*, 429, 139 (CL94)
- Crenshaw, D. M., & Kraemer S. B. 2007, *ApJ*, 659, 250
- Dorodnitsyn, A., Kallman, T., & Proga, D. 2008, *ApJ*, 675, L5
- Ferrarese, L. & Merrit, D. 2000, *ApJ*, 539, L5
- Elvis, M. 2000, *ApJ*, 545, 63
- Everett, J. E. 2005, *ApJ*, 631, 689
- Grevesse, N., Noels, A., & Sauval, A. 1996, in “Cosmic Abundances” ASP Conference Series, 99, S. Holt and G. Sonneborn, eds.
- Grupe, D. et al. 2004, *AJ*, 127, 1799
- Haardt, F., & Maraschi, L. 1991, *ApJ*, 380, L51
- Hanke, M. et al. 2009, *ApJ*, 690, 330

- Holczer, T., Behar, E. & Kaspi, S. 2007, ApJ, 663, 799 (HBK07)
- Holczer, T., Behar, E. & Arav, N. 2009, (submitted to ApJ)
- Hopkins, P. F. et al. 2005, ApJ, 630, 705
- Hua, X.-M., Kazanas, D. & Titarchuk, L. G. 1997, ApJ, 482, L57
- Kazanas, D., Hua, X.-M. & Titarchuk, L. G. 1996, ApJ, 480, 735
- Kallman, T., & Bautista, M. 2001, ApJS, 133, 221
- Kawanaka, N., Kato, Y., & Mineshige, S. 2008, PASJ, 60, 399
- Köngl, A. & Kartje, J. F. 1994, ApJ, 434, 446 (KK94)
- Kotani, T. et al. 2000, ApJ, 539, 413
- Kraemer, S. B. et al. 2005, ApJ, 633, 693
- Krolik, J. H. & Begelman, M. C. 1988, ApJ, 329, 702
- Lynden-Bell, D. 1969, Nature, 223, 690
- Mihalas, D. 1978, “Stellar Atmospheres”, W. H. Freeman & Company, New York, NY, 2nd edition, p. 279
- Miller, J. M. et al. 2006, Nature, 441, 953
- Miller, J. M., Raymond, J., Reynolds, C. S., Fabian, A. C., Kallman, T. R., & Homan, J. 2008, ApJ, 680, 1359
- Murray, N., & Chiang, J. 1998, ApJ, 494, 125
- Nandra, K. et al. 1998, ApJ, 505, 594
- Narayan, R., & McClintock, J. E. 2008, New Astron. Rev., 51, 733
- Narayan, R. & Yi, 1994, ApJ, 428, L13
- Narayan, R. & Yi, 1995a, ApJ, 444, 231
- Narayan, R. & Yi, 1995b, ApJ, 454, 710
- Ohsuga, K., Mineshige, S., Mori, M., & Kato, Y. 2009, PASJ, 61, L61
- Papadakis, I. E., Nandra, K. & Kazanas, D. 2001, ApJ, 544, L133

- Pounds, K. A. & Reeves, J. N. 2009, MNRAS, 397, 249
- Proga, D. 2003, ApJ, 585, 406
- Proga, D. & Kallman, T. R. 2004, ApJ, 616, 688
- Reeves, J. N., O’Brien, P. T., Braito, V., Behar, E., Miller, L., Turner, T. J., Fabian, A. C., Kaspi, S., Mushotzky, R., & Ward, M. 2009, ApJ, 701, 493
- Reynolds, C. S. & Fabian, A. C. 1995, MNRAS, 273, 1167
- Risaliti, G. & Elvis, M. 2004, in “Supermassive Black Holes in the Distant Universe”, Ed. A. J. Barger, Kluwer Academic Publishers, Dordrecht, The Netherlands, 2004, p.187
- Sanders, D. B. et al. 1989, ApJ, 347, 29
- Schurch, N. J. & Done, C. 2007, MNRAS, 381, 1413
- Schurch, N. J., Done, C. & Proga, D. 2009, ApJ, 694, 1
- Sim, S. A. 2005, MNRAS, 356, 531
- Sim, S. A., Long, K. S., Miller, L., & Turner, T. J. 2008, MNRAS, 388, 611
- Tueller, J. et al. 2008, ApJ, 681, 113
- Ueda, Y., Akiyama, M., Ohta, K., & Miyaji, T. 2003, ApJ, 598, 886
- Urry, M. C. & Padovani, P. 1995, PASP, 107, 803
- Young, A. J., Lee, J. C., Fabian, A. C., Reynolds, C. S., Gibson, R. R., & Canizares, C. R. 2005, ApJ, 631, 733